Deformation of the Ultra-High Molecular Weight Polyethylene Melt in the Plane-Strain Compression

Zbigniew Bartczak,[1] Petra F. M. Beris,[2] Krzysztof Wasilewski,[1] Andrzej Galeski,[1] Piet J. Lemstra[2]

[1]*Centre of Molecular Macromolecular Studies, Polish Academy of Sciences, Sienkiewicza 112, 90-363 Lodz, Poland*
[2]*Department of Chemical Engineering, Dutch Polymer Institute/Eindhoven University of Technology, Eindhoven 5600 MB, The Netherlands*

Received 30 November 2011; accepted 30 November 2011
DOI 10.1002/app.36595
Published online in Wiley Online Library (wileyonlinelibrary.com).

ABSTRACT: Deformability of molten ultra-high molecular weight polyethylene (UHMWPE) was studied in the plane-strain compression at the temperature from a range of 145–165°C. Two grades of UHMWPE were tested—a commercial one synthesized in a slurry process with conventional Ziegler-Natta catalyst and the material polymerized in solution at low temperature using a homogeneous metallocene catalyst. These grades differ markedly in the initial concentration of chain entanglements in nascent powders. Specimens used for compression were produced either by compression molding or compaction of the nascent powders (sintering) at the temperature up to 130°C in order to obtain a set of samples with a range of chain entanglement concentration. Plane-strain compression tests demonstrated a rubber-like behavior and a good deformability of molten samples in the temperature range of 145–155°C. The ultimate true strain up to $e = 3$ was observed in samples prepared by compression molding, while for sintered samples of metallocene polymer it exceeded $e = 4.3$ (deformation ratio, $\lambda > 74$). At higher temperature of 165°C deformation became unstable. A strong correlation between topological structure of the melt and its deformation behavior was found: highly disentangled samples (from nascent powder of metallocene polymer) tend to deform to much higher strain than samples of lightly reduced concentration of chain entanglements (from nascent powder of commercial Z-N polymer) or samples with entanglement density close to an equilibrium (prepared by compression molding), which demonstrated the lowest ultimate strain. The obtained results point out a new route of melt-processing of UHMWPE nascent powders for fabrication of ultra-strength fibers, alternative to the gel-spinning technology. © 2012 Wiley Periodicals, Inc. J Appl Polym Sci 000: 000–000, 2012

Key words: compression; melt; entanglements; polyethylene; UHMWPE

INTRODUCTION

Macromolecules of synthetic polymers demonstrate usually considerable length and flexibility. Due to that the chains in a molten polymer are highly entangled. This, in turn, leads to a high viscosity of polymer melts, which increases strongly with increasing molecular weight. Such an increase of viscosity sets a limit on processability of polymers on the high molecular weight side. Since the properties of polymers in the solid state usually improve with increasing molecular weight, notably the strength and toughness, the melt-processing of thermoplastic polymers, e.g., injection-molding, extrusion, fiber spinning, is often a compromise between the ease of processing (lower molecular weight preferred due to easier flow) and properties (preference for high molecular weights). In an ultimate case of polymers of very high molecular weight, as ultra-high molecular weight polyethylene (UHMWPE; $M_w \sim 10^6$) the melt-processing becomes practically impossible and solution technologies must be used instead. The melt-processability of such materials can be restored only if the number of entanglements is greatly reduced.

Entangling of polymer chains is a spontaneous process, therefore, it is difficult to control the concentration of entanglements in the polymeric material. However, in the case of semicrystalline polymer the number of entanglements persisting in the amorphous phase after sample crystallization actually depends on the conditions of crystallization process and therefore can be modified in a limited range. For example, the density of entanglements can be considerably reduced in samples crystallized carefully from dilute solution, [1–3] or in samples of relatively low molecular weight crystallized very slowly from the melt.[4] In dilute solutions, below the overlap concentration φ^*, entanglements can be removed almost completely. This highly reduced entanglement density can be fixed by careful crystallization,

Correspondence to: Z. Bartczak (bartczak@cbmm.lodz.pl).
Contract grant sponsor: Ministry of Science and Higher Education of the Republic of Poland; contract grant number: 3 T08E007 28

resulting in regularly chain-folded crystals. Ability of some polymers to crystallize in chain-extended fashion under elevated pressure, like PE or PVDF, also allows for reduction of the number of entanglements at appropriate conditions of crystallization.[5] Another possibility of fabrication of material with low density of entanglements offers crystallization during polymerization.[6] In commercial processes, UHMWPE is synthesized by a slurry process using a Ziegler-Natta catalyst and a hydrocarbon diluent. As the active sites in such catalyst systems are relatively close together, the chains grow in close proximity to each other. Due to the relatively high polymerization temperature of 60–100°C, crystallization of the polymer chains is slow compared to the polymerization. These conditions facilitate formation of entanglements during synthesis, although their concentration is slightly reduced in comparison to an equilibrium melt. However, it is possible to obtain a much less entangled system directly in the reactor, by an appropriate modification of polymerization conditions, e.g., decreasing number of active sites or using a single site catalyst,[7] and/or decreasing polymerization temperature well below the crystallization temperature (polymerization rate becomes then lower than crystallization rate)—it is ultimately possible to reach the state when growing chains are separated far enough from each other while crystallization proceeds simultaneously with polymerization. This results in an independent growth of "monomolecular" crystals (a single chain forming a single crystal) what reduces greatly the concentration of chain entanglements.[8,9] Several nascent reactor powders of polyethylene have been recognized to be drawable at temperatures below the melting temperature, which was associated to a reduced number of entanglements.[9–11]

At certain conditions the disentangled state of the pressure-crystallized PE or nascent powders can be maintained in the melt for a period of time,[12] which is needed for a macromolecule to reptate to the entirely new position. That time may be roughly estimated as much more than 10^4s for UHMWPE.[13,14] During that period the UHMWPE melt demonstrates reduced viscosity,[14] which greatly improves processability. This feature opens a limited time window for melt-processing of UHMWPE. The purpose of this study was to explore such a possibility of melt-processing of the nascent powders of UHMWPE. In particular, we have been interested in production of high molecular orientation in the melt obtained directly from a nascent reactor powder. Two reactor powders produced at very different polymerization conditions and of different thermal history were tested. Orientation of the molten samples was produced by plane-strain compression.

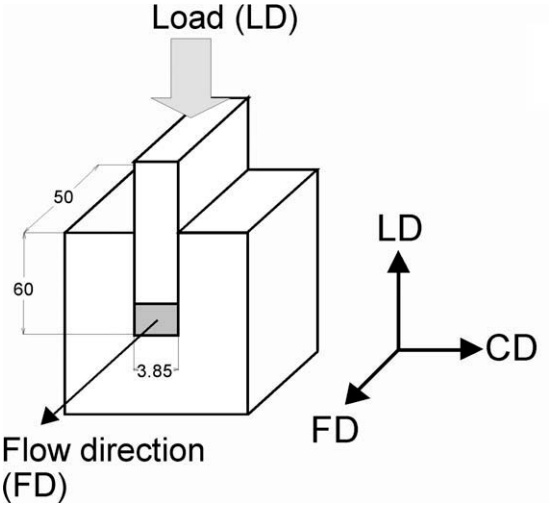

Figure 1 Schematic view of a channel-die used for deformation experiments. The compressed sample is marked with gray. LD, FD and CD denote the directions of loading, material flow and constraints, respectively.

MATERIALS AND METHODS

Materials

The materials used in this study were nascent reactor powders of the commercial ultra-high molecular mass polyethylene (UHMWPE) Hostalen GUR 4150, provided by Ticona GmbH, with the density of 0.930 and molecular weight of $M_w \sim 6.5 \times 10^6$ and UHMWPE polymerized in the lab using a homogeneous metallocene FI catalyst and MAO as an activator. The polymerization was carried out at $T = 15$°C and ambient pressure. The molecular weight estimated from rheometric measurements is about $M_w = 6 \times 10^6$.

Samples in the form of 3.65-mm thick plates were prepared by hot compaction (sintering) of the powders in a dedicated mould at the temperature $T =$ 100–130°C and the pressure $p =$ 200–400 bar for 30 min. The reference samples were prepared from the same powders by their melting and compression molding at $T = 220$°C and $p = 100$ bar for 10 min. The molded plates were solidified by fast cooling. Specimens of the size desired for deformation experiments were machined out from the prepared plates.

Compression

Plane-strain compression tests were performed using a loading frame of an universal tensile testing machine (Instron, Model 5582, controlled by the Bluehill II software) and a compression tool of the type of a deep channel-die, equipped with a load and strain gauges as well as heaters connected to the temperature controller. The channel-die is shown schematically in Figure 1. The temperature of the channel-die was kept during the deformation

experiment at the desired value (room temperature, 120°C, 145°C, 155°C, or 165°C) with an accuracy better than 0.5°C. The size of the specimens used were $20 \times 50 \times 3.65$ mm^3 [along the load direction (LD), flow direction (FD), and constrain direction (CD), respectively]. The solid specimen (compacted powder or compression molded) was placed in the channel-die preheated to the deformation temperature. After 10 min. period necessary for polymer melting and temperature equilibration, the molten specimen was deformed with the constant true strain rate of 0.1, 0.01, or 0.001 s^{-1}. The true strain (Hencky strain) was calculated with the formula:

$$e = \ln \lambda = \ln(h_o/h) \quad (1)$$

where $\lambda = h_o/h$ is the compression ratio (h_o and h denote the initial and actual sample height, respectively). To maintain the constant true strain rate, the speed of the crosshead had to be adjusted (reduced) accordingly as the actual sample height decreased during the compression test. The crosshead speed was controlled by the software of the testing machine (Bluehill II by Instron Corp.) on the basis of the actual sample height measured by the strain gauge.

After compression, the crosshead of the testing machine was stopped and the heaters were switched off to allow the sample crystallize at constant height (under load). Other details of compression in channel-die are given in the Ref. 15.

DSC

Thermal analysis was conducted using a TA 2920 DSC apparatus (Thermal Analysis). The melting thermograms were recorded at the heating rate of 10°/min, under nitrogen flow. The crystallinity was estimated on the basis of heat of melting of the sample, assuming the heat of melting of 100% crystalline PE of $\Delta h_f = 293$ J/g.[16]

SAXS

Lamellar structure of deformed samples was probed by a 2-D small angle X-Ray scattering (2-D SAXS). A 1.1 m long Kiessig-type camera was equipped with a tapered capillary (XOS) and pinhole collimator and an imaging plate as a detector (Fuji). The camera was coupled to a X-ray generator (sealed-tube, fine point CuK$_\alpha$ filtered source operating at 50 kV and 30 mA; Philips). Exposed imaging plates were read with Phosphor-Imager SI scanner (resolution 50×50 μm^2) and the ImageQuant software (Molecular Dynamics). For determination of the long period one-dimensional sections of recorded 2-D patterns were extracted. Background and Lorentz correction were applied to obtained curves. If the corrected curve exhibited a maximum the long period was estimated from position of that maximum using the Bragg law.

WAXS

The texture of deformed samples was studied using the X-ray pole figure technique (for overview of this technique see e.g., Ref. 17). A WAXS system consisted of a computer controlled pole figure attachment associated with a wide angle goniometer coupled to a sealed-tube source of filtered CuK$_\alpha$ radiation, operating at 50 kV and 30 mA (Philips). The specimens in the form of slices $\sim$ 2 mm thick were cut out from the deformed samples in the plane perpendicular to the flow direction (FD). The other details of pole figure preparation was described elsewhere.[18] The following diffraction reflections from orthorhombic crystal form of PE were analyzed: (110), (200), and (020), positioned at $2\Theta = 21.6^o$, 24.0^o, and 36.4^o, respectively.

To analyze quantitatively the preferred orientation developed in oriented samples, the Herman's orientation factor was additionally calculated. The orientation factor is defined as:

$$f = \frac{3\langle \cos^2 \varphi \rangle - 1}{2} \quad (2)$$

where φ is the angle between a direction of interest within the crystal (e.g., chain axis, **c**) and the reference axis (e.g., the flow direction). The average square cosine of the angle between normal to a chosen (*hkl*) plane and the flow direction (FD), $\langle \cos^2 \varphi_{hkl} \rangle$ can be determined from the same diffraction intensity data used for construction of the respective pole figure, using the following equation[17]:

$$\langle \cos^2 \varphi_{hkl} \rangle = \frac{\int_0^{2\pi} \int_0^{\pi/2} I(\varphi, \psi) \cos^2(\varphi) \sin \varphi \, d\varphi \, d\psi}{\int_0^{2\pi} \int_0^{\pi/2} I(\varphi, \psi) \sin \varphi \, d\varphi \, d\psi} \quad (3)$$

where φ and ψ are the polar angle and the azimuth in the respective (*hkl*) pole figure. From average cosines of two paratropic planes (110) and (200) the $\langle \cos^2 \varphi_c \rangle$ was calculated with Wilchinsky's method[19]:

$$\langle \cos^2 \varphi_c \rangle = 1 - 1.445\langle \cos^2 \varphi_{110} \rangle - 0.555\langle \cos^2 \varphi_{200} \rangle \quad (4)$$

and then the Herman's orientation factor f_c was calculated with eq. (2). This orientation factor describes an orientation of the crystallographic **c** axis (equivalent to the chain axis) around FD. It is equal to 1 for a perfect orientation of chains along FD, $-1/2$

TABLE I
Thermal properties of the samples studied evaluated from DSC data.

Sample	Preparation	$T_{m,\text{onset}}$ (°C)	T_m (°C)	X_c (wt %)
G-np	Nascent powder	133.5	142.1	61.4
P-np	Nascent powder	133.3	140.3	78.4
G-S_{100}	Sintered at 100°C	134.1	143.5	65.2
G-S_{130}	Sintered at 130°C	134.8	144.5	69.0
P-S_{100}	Sintered at 100°C	133.6	142.7	84.6
G-M	Compression molded at 220°C	124.5	132.8	48.9

for precise perpendicular orientation and 0 for a random orientation.

Rheology

The rheological measurements were executed with the Ares LS oscillatory rheometer (TA Instruments) with parallel plate geometry (steel plates of 8 mm in diameter). The temperature of 160°C, strain of 1%, and frequency of 10 rad/s were used. The moduli G', G'' and the phase angle were measured at constant temperature and frequency as a function of time. Estimation of the modulus build-up time from the G' vs. time curve allows to determine whether the sample was initially disentangled: a disentangled sample shows a build-up of modulus, while fully entangled sample does not.

RESULTS AND DISCUSSION

Characterization of samples

Thermal properties of the samples studied were evaluated from the melting thermograms obtained with DSC. Table I presents temperatures of the onset of melting $T_{m,\text{onset}}$, temperature of the melting peak T_m, and the crystallinity degree, determined for initial nascent powders (commercial sample, obtained with Ziegler-Natta catalyst; denoted G-np, and the laboratory sample, polymerized with homogeneous catalyst at low temperature; P-np), sintered samples (G-S and P-S, respectively) and the compression molded sample of commercial UHMWPE (G-M) as a reference.

The presented data reveal high crystallinity and very high melting point of nascent powders of both G and P grades. Crystallinity of the nascent powder of the experimental sample P-np (homogeneous catalyst, low temperature of polymerization) is considerably higher than the commercial sample G-np (Z-N catalyst), 78 vs. 61 wt % respectively, which probably reflects its supermolecular structure consisting of monomolecular crystals and reduced number of chain entanglements.

The melting temperature of nascent crystals of both polyethylene grades studied is very high, above 140°C, i.e., temperature normally found for "chain-extended" polyethylene crystals, which are extremely thick (up to few μm). Such a high temperature of melting of nascent crystals was explained as an effect of strong constraints imposed on these crystals by adjacent amorphous regions, which lead to different kinetic of melting comparing to the melt-crystallized crystals.[20] Consequently, melting of such strongly constrained crystals is postponed on heating with a finite rate to temperatures higher than observed for regular crystals of similar thickness. The high melting point was also associated with a possible presence in nascent samples a relatively small fraction of very thick crystals of partially extended chains.[21] Nascent powder of the experimental sample P-np exhibits a lower melting point than the commercial powder G-np, which again points out a supermolecular structure of this sample with weaker constraints imposed on crystals by amorphous neighborhood exhibiting fewer chain entanglements than the G-np powder.

After sintering at $T = 100$°C or 130°C, i.e., still below the onset of melting of nascent powders ($T_{\text{ons}} > 133$°C), both the melting temperature and crystallinity increased markedly due to annealing effect. The crystallinity of the experimental sample sintered at 100°C P-S_{100} increased from $\sim$ 78 wt % to nearly 85 wt %, while the crystallinity of commercial grade G increased from 61 wt % to 65 and 69 wt % in samples sintered at 100°C and 130°C, respectively. The nascent form of experimental sample P was obtained by crystallization of chains directly upon synthesis using homogeneous catalyst. As the temperature of polymerization was kept low, the growing chains crystallized immediately. Fast crystallization of polymer chains upon formation in combination with sufficient dilution kept the growing and immediately crystallizing chains apart which facilitated formation of monomolecular crystals and consequently a polymer powder with greatly disentangled chains.[8,9] On the other side, the commercial G grade is synthesized in a slurry process using Ziegler-Natta catalyst. Because of small distances between active sites the chains grow close each to the other, while the crystallization rate is low compared to the polymerisation rate due to relatively high temperature (60–100°C). Such conditions favour formation of crystallites composed of many different chains and entangling of these chains in adjacent amorphous layers. Consequently, the average number of entanglements per unit chain in the nascent G sample is expected higher than in the metallocene sample P, although probably still lower than in the melt- crystallized material. The high crystallinity values, increasing considerably on annealing (sintering)

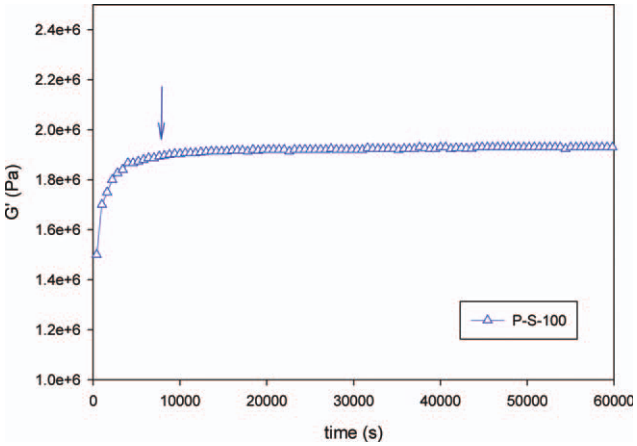

Figure 2 Modulus built-up in the melt of the nascent powder sample of experimental UHMWPE, P-S-100 of reduced entanglement concentration at T=160°C. Arrow in the figure corresponds to the built-up time, when $G'/G_{nN} = 0.98$. [Color figure can be viewed in the online issue, which is available at wileyonlinelibrary.com.]

below the melting point, faster in P than in G, seem to confirm the above picture.

Considerably, disentangled state of the nascent powder as well as sintered sample of P grade was confirmed by a rheological measurements of build-up of the modulus G' with time (cf. Fig. 2).

For the sample of sintered powder of the metallocene polymer P melted slowly in the rheometer and then kept at 160°C, the shear modulus G' recorded at this temperature initially increased gradually from 1.5 to nearly 2.0 MPa and reached a nearly constant value after $\sim 10^4$ s of annealing. In a thermodynamically stable melt having a homogeneous distribution of entanglements the shear modulus in the rubbery plateau is related to entanglements[22]:

$$G_{0N} = \rho RT/\langle M_e \rangle \quad (5)$$

where ρ is the density, R is the gas constant, T is the absolute temperature, and $\langle M_e \rangle$ is the average molecular weight between entanglements, inversely proportional to the entanglement density, N_e. It can be assumed that this equation holds qualitatively also in the non-equilibrium case of the melt with reduced concentration and heterogeneous distribution of entanglements, which is considered here.[14] It was demonstrated[20,23] that the distribution of entanglements in the partially disentangled sample after its melting is heterogeneous, especially, when the sample melted slowly. The results obtained for the sample P (Fig. 2) may suggest then a gradual increase of entanglements concentration due to diffusion/reptation on melt-annealing. When chains reach the equilibrium entangled state the modulus approaches its asymptotic value. The time necessary for that can be estimated as approximately $\tau \sim 10^4$ s.

The sintered sample G-S, tested at the same conditions, demonstrated merely a minor initial changes in modulus, which can suggest that concentration of entanglements in the nascent powder of the G grade is only a slightly reduced as compared to the equilibrium state. The control compression molded sample G-M did not revealed any evolution of modulus with time, which confirms concentration of entanglements close to equilibrium.

Melting of a nascent powder on compression molding at 220°C and its recrystallization on subsequent cooling results in a decrease of both the melting temperature and overall crystallinity. Melting point of G-M sample lowers below 133°C, a value typical for chain-folded crystals linear polyethylene crystallized from the melt. Entanglements present already in the structure as well as those newly created on melting, redistributed homogeneously during melt-annealing on compression molding hinder the growth of crystallites and consequently the crystallinity of the G-M sample does not exceed 50 wt %.

Stress–strain behavior

Figure 3 presents the true stress–true strain curves obtained for G and P samples prepared by sintering (T = 100°C, samples G-S and P-S, respectively) or compression molding (T = 220°C, samples G-M) and deformed by plane-strain compression. Samples were deformed with the constant true strain rate of

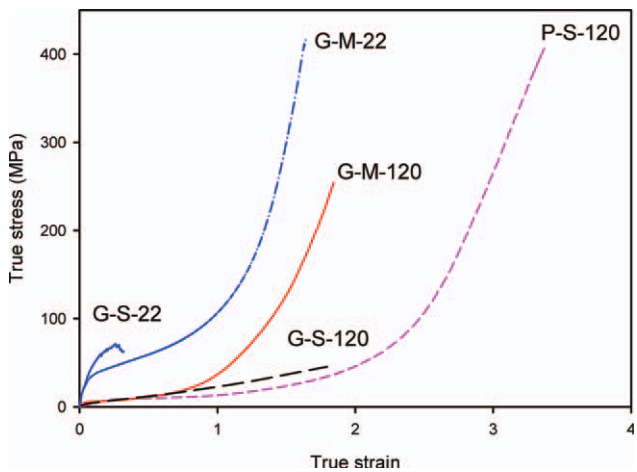

Figure 3 The true stress – true strain curves of UHMWPE samples deformed at room temperature and at 120°C with the true strain rate, $de/dt = 0.01s^{-1}$. Sample codes: G-S-22: polymer G (commercial), nascent powder sintered at 100°C, deformed at room temperature; G-S-120: the same, deformed at T=120°C; G-M-22: polymer G, molded at 220°C, deformed at room temperature;G-M-120: the same, deformed at T = 120°C; P-S-120: polymer P (laboratory), nascent powder sintered at 100°C, deformed at T = 120°C. [Color figure can be viewed in the online issue, which is available at wileyonlinelibrary.com.]

0.01 s^{-1} either at room temperature or at T_{def} = 120°C, i.e., well below the melting point of the crystalline phase. It was found that sintered samples deformed at room temperature fractured early, near the yield point, due to poor connectivity between crystallites and/or grains of the powder. Sample P-S fractured even in the elastic range, earlier than G-S, due to higher crystallinity and probably poorer connectivity between crystals. In contrast, the compression molded samples tested at room temperature deformed plastically up to relative high true strain, e = 1.6 (compression ratio $\lambda \sim 5$), with a distinct strain hardening stage, leading to very high ultimate stress of 400 MPa (see the curve of G-M-22 in Fig. 3). This change of the deformation behavior reflects significantly higher connectivity between crystallites as well as much better fusing of grains of the powder due to sample processing in the molten state.

At the temperature of T_{def} = 120°C (samples were still solid as $T_{def} < T_m$) deformation of G and P polymers (either compression molded or sintered) proceeded to considerably higher true strain, up to around e = 3 (compression ratio, λ = 20). The modulus and the yield stress were, as expected, lower than those observed at room temperature. Additionally, one could observe distinct changes in the plastic flow and strain hardening stages, especially in sintered materials. These stages of deformation in compression molded samples G-M proceed similarly at T_{def} = 120°C and the room temperature, although at lower stress level (reduced by the lowered contribution of the crystalline component). An onset of strain hardening was observed around e = 0.6–0.8 at both temperatures. This is because the strain hardening is controlled primarily by the properties of the molecular network in the amorphous component (concentration of entanglements),[15] which are very similar at both temperatures (in initial stage of the strain hardening the contribution of the global reorganization of the chain coils including the chain stems in the deforming crystalline component to the strain hardening is much smaller[15,24,25]). In contrast, the P-S sintered sample exhibited much longer flow stage and the strain hardening was delayed to the true strain near e = 2. In the strain hardening stage, the stress increased strongly to σ = 400 MPa at e = 3.3. Sintered sample of commercial UHMWPE, G-S tested at 120°C exhibited the stress at similar level as molded G-M sample up to the strain of e = 0.6, yet did not demonstrate the strong stress hardening stage as other samples did. It deformed further up to the true strain approaching 2 with only moderate increase of the stress, still below 100 MPa. It can be guessed that fracture occurs in this material before strong strain hardening set in, possibly due to weak grain boundaries.

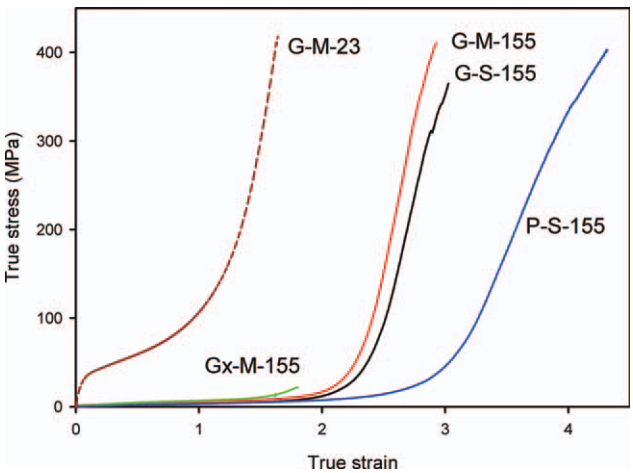

Figure 4 The true stress – true strain curves of UHMWPE samples deformed at T_{def} = 155°C with the strain rate, de/dt = 0.01s^{-1}. Sample codes: G-M-155: polymer G, molded at 220oC, deformed at T = 155°C; Gx-M-155: polymer G, compression molded at 220°C and cross-linked by irradiation (dose 50kGy), deformed at T = 155°C; G-S-155: polymer G, nascent powder sintered at 100°C, deformed at T = 155°C; P-S-155: polymer P (laboratory), nascent powder sintered at 100°C, deformed at T = 155°C. As a reference the curve of G-M-22 (polymer G molded at 220°C and deformed at room temperature) is presented. [Color figure can be viewed in the online issue, which is available at wileyonlinelibrary.com.]

In Figure 4, the stress–strain curves obtained for samples deformed at T_{def} = 155°C are presented. At this temperature all samples were completely molten. It can be observed that all of them show similar stress–strain behavior with very low stress up to e = 2 and pronounced strain hardening stage above this strain. The flow stress observed below strain hardening is much lower than in samples deformed at room temperature since there is no contribution of the crystalline phase—crystals melted completely below the deformation temperature. Significant strain hardening can be observed at $e > 2$ in G-M and G-S samples of the commercial G polymer. Sintered sample G-S exhibits strain hardening shifted slightly towards higher strain as compared to compression molded sample G-M. The fracture of G-M and G-S occurs at the strain around e = 2.8 and 3.0, respectively (compression ratio λ = 16 and 20) and the true stress above 350 MPa. The larger deformability of the sintered sample can be accounted for slightly reduced concentration of entanglements in the sintered sample containing nascent structures as compared to its compression molded counterpart. For comparison, the curve of compression molded sample Gx-M, in which the amorphous phase was highly cross-linked with an electron beam irradiation (dose of 50 kGy; insoluble gel fraction of 97%), is also presented. At T_d = 155°C this sample deformed initially in similar fashion as

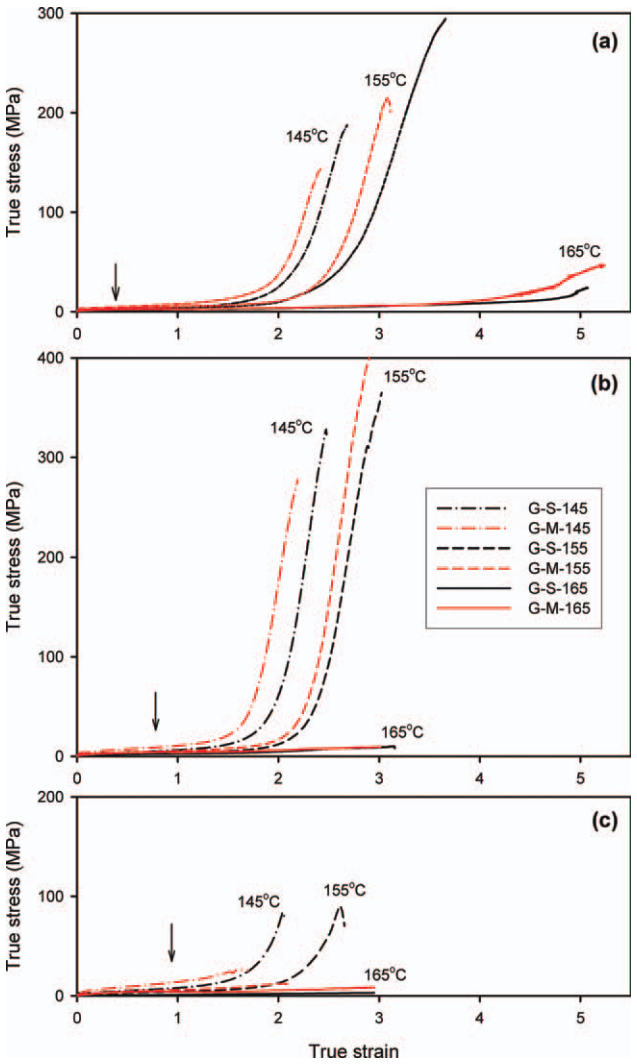

Figure 5 True stress – true strain compression curves obtained for samples deformed at the strain rate of: 0.001 s^{-1} (a), 0.01 s^{-1} (b) and 0.1 s^{-1} (c). Temperature of deformation indicated for each curve. [Color figure can be viewed in the online issue, which is available at wileyonlinelibrary.com.]

G-M and G-S samples, yet fractured at the strain of merely $e = 1.7$, just on the beginning of the strain hardening, because of much lower stretching limit of the molecular network composed of highly cross-linked chains as compared to the network of entangled chains in G-M or G-S.

Highly disentangled metallocene sample P-S tested at $T_{def} = 155°C$ was able to deform to much higher strain than any sample of G grade. It demonstrated easy flow without much stress built-up to the strains well above $e = 2.5$ and was able to deform further in the strain hardening range, reaching finally the true strain of $e = 4.3$ (deformation ratio $\lambda > 74$) at the stress of 400 MPa. The much extended flow region of this sample indicates an increased stretching limit of the molecular network which is a result of the reduced entanglement density in this sample. For the network of low entanglement density, the resolving of entanglements due to flow is also easier than in more dense network of G-S.

Figure 5(a–c) present the true stress–true strain curves of plane-strain compression obtained for molten G-M (compression molded) and G-S (sintered) samples. These curves were produced at various temperatures of deformation (145, 155, and 165°C) and deformation rates [$de/dt = 0.001$, 0.01, and 0.1 s^{-1}; cf. Fig. 5(a–c), respectively]. At the deformation temperature 145°C some traces of the crystalline structure could be still present in the sample, especially in sintered specimens, demonstrating the maximum of the melting peak at $T = 142.7$–$144.5°C$ (cf. Table I), while at $T_{def} = 155°C$ or 165°C all samples were completely molten prior to compression. At both deformation temperatures, 145°C and 155°C, a strain induced crystallization can take place.[1,26] At the highest deformation temperature used, $T_{def} = 165°C$, the orthorhombic-hexagonal solid–solid phase transition under load is additionally possible.[27] Tensile experiments performed for molten UHMWPE demonstrated limited drawability of the melt at temperatures up to 155°C and a failure of the material at low tensile strains when the deformation temperature was higher.[1,26]

The stress–strain curves obtained at $T_{def} = 145°C$ and 155°C demonstrate a characteristic shape indicating a rubber-like behavior with a very intense strain hardening, followed by the rupture of the sample at the true strain above $e = 2$. The stress in the plastic flow region increased, as expected, with an increasing deformation rate due to an increase of viscous forces with an increasing strain rate. An increase of viscous forces led also to the premature fracture of samples compressed with the highest strain rate used, $de/dt = 0.1$ s^{-1}. At this rate G-M samples tend to fracture even prior to stress hardening. G-S samples tested at the same rate usually reached the strain hardening stage, yet fractured at relative low strain and stress, below 100 MPa ($T_{def} = 145$–$155°C$), much smaller than on compression with lower strain rates. Such a behavior, including a high sensitivity to the strain rate, confirms a postulated difference in the topological structure of G-S and G-M samples, consisting of molecular network of entangled chains with different concentration of entanglements—as the melt viscosity is dependent on entanglement density the viscous forces generated on deformation of less entangled G-S sample are smaller, which facilitates higher deformation of G-S than G-M.

The samples tested at $T_{def} = 165°C$ demonstrate an opposite behavior to those deformed at lower temperature—stress–strain curves do not show any strain hardening. They exhibit instead some flow instabilities already at relative low strains, in the form of small drops of the stress, frequently

TABLE II
Ultimate True Strain, e_b, and Ultimate True Stress, σ_b of Samples of the G-Grade UHMWPE Deformed at Various Temperatures and Deformation Rates

Sample	Temperature of deformation (°C)	$de/dt = 10^{-3}$ s^{-1}		$de/dt = 10^{-2}$ s^{-1}		$de/dt = 10^{-1}$ s^{-1}	
		e_b	σ_b (MPa)	e_b	σ_b (MPa)	e_b	σ_b (MPa)
G-M	145	2.5	140	2.2	280	1.6	27
	155	3.1	210	2.8	400	2.1	10
	165	~ 5	40	3.0	10	2.8	8
G-S	145	2.7	185	2.5	330	2.1	85
	155	3.7	295	3.1	365	2.7	90
	165	~ 5	20	3.1	10	2.9	9

followed by a fast rise to the previous stress level. These stress instabilities were probably induced by small-scale local fracture of the molten sample, followed by an immediate healing of the crack due to compressive stress components. Such features were frequently observed already at strains well below 1.0 [indicated by arrows in plots of Fig. 5(a–c)]; lower the deformation rate the smaller the strain at which first instabilities were observed. The final, macroscopic rupture of samples deformed at 165°C occurred much later, at the true strain above 3, especially in samples deformed with the lowest strain rate of 0.001 s^{-1}, which broke around $e \sim 5$ [cf. Fig. 5(a)]. The ultimate stress reached in samples compressed at 165°C was always low, much below 50 MPa, independently of the strain rate. The flow instabilities observed at relative low strain confirm that large-strain deformation of the molten UHMWPE at temperature above 155°C is difficult or practically impossible not only in tension, as already reported,[1,26] but also in plane-strain compression studied here.

The ultimate true strain and ultimate true stress of the samples of G grade determined from the stress–strain curves are summarized in Table II. Data presented in Figure 5 and Table II indicate that melt-processed samples G-M show always an earlier onset of the strain hardening and fracture at lower strains than sintered G-S counterparts deformed at the same conditions, in the entire range of deformation temperature and strain rate studied. Since the strain hardening is controlled primarily by the properties of the network of entangled chains[15] it can be concluded that the reported features are related directly to the entanglements density, which is undoubtedly lower in the sintered samples G-S than in melt-processed samples G-M.

The experimental stress–strain curves were fitted with model curves calculated on the basis of simple one-dimensional model,[15] involving a viscous flow and a rubber-elastic response of the molecular network, based on the hypothesis of Haward and Thackray.[28] According to this hypothesis strain hardening originating from stretching of the molecular network of entangled chains can be represented in the model by the non-linear spring element, connected in parallel with a viscoplastic dashpot representing the rate and temperature dependent yield and plastic and viscous flow. Since the primary interest was focused on the response of the molecular network several simplifying assumptions were allowed here in the model formulation: the material was assumed incompressible, and its viscoplastic response was represented by a single disposable stress parameter. Any dependence of it on the strain rate and temperature were not considered. Moreover, any molecular relaxation phenomena within the network or flow-induced evolution of the network (resolving of a part of entanglements) were not taken into account, while in the real system such processes can accommodate some of the imposed strain. Finally, the stress-induced crystallization which can occur on late stages of the deformation process was also neglected. Under such assumptions the true stress generated in the plane-strain geometry can be simply represented by the sum[15,29]:

$$\sigma_{e+n} = \sigma_{\mathrm{fl}} + \sigma_R \tag{6}$$

where σ_{fl} is the viscoplastic stress related to the flow and σ_R is the elastic rubber-like stress generated by the molecular network. The network stress σ_R was modeled using a non-Gaussian chain statistics and the 8-chain model developed by Arruda and Boyce.[30] For the plane-strain compression geometry, the equation for the stress in the direction of loading takes the form[15]:

$$\sigma_R = \frac{N_{\mathrm{eff}} kT}{3} \sqrt{n} \frac{1}{\lambda_{\mathrm{chain}}} L^{-1}\left(\frac{\lambda_{\mathrm{chain}}}{\sqrt{n}}\right) \cdot \left(\lambda^2 - \frac{1}{\lambda^2}\right) \tag{7}$$

where N_{eff} is the effective network density (in the case of polymer melt it is equal to the number of chain entanglements active during deformation of the network, calculated per unit volume), n is the number of "rigid links" between entanglements providing an extensibility limit of a chain in an initial network ($\lambda_{\max} = n^{1/2}$) and λ_{chain} is the stretch on each chain in

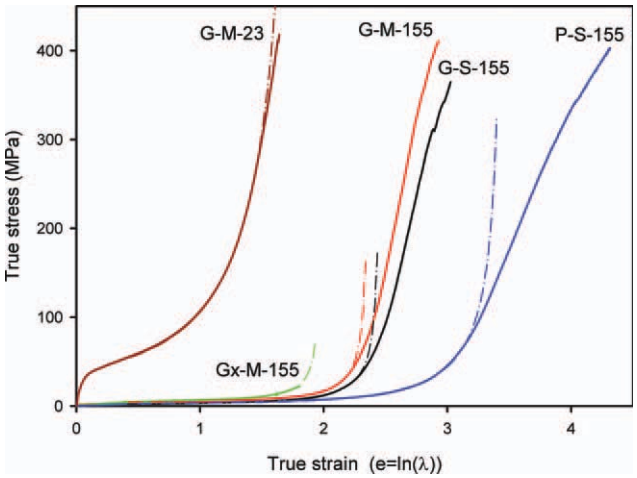

Figure 6 Comparison of experimental stress-strain curves (solid lines) and fitted with eqs. (6)-(7) (broken lines) for samples deformed at T = 155°C and de/dt=0.01 s^{-1}. [Color figure can be viewed in the online issue, which is available at wileyonlinelibrary.com.]

the network, given by the root mean square of the applied strain; for plane strain compression $\lambda_{chain} = [1/3\ (\lambda^2+1+1/\lambda^2)\ ]^{1/2}$, where $\lambda = CR = h_o/h$ is the compression ratio. $L^{-1}(x)$ denotes the inverse Langevin function [$L(x) = \coth(x) - 1/x$; here $x = \lambda_{chain}/n^{1/2}$]. The quantity N_{eff} kT is equivalent to the initial strain hardening modulus of the network, G_n. For large values of n, eq. (5) reduces to the simple Gaussian equation (plane-strain conditions):

$$\sigma_R = G_n\left(\lambda^2 - \frac{1}{\lambda^2}\right) \tag{8}$$

where $G_n = N_{eff}$ kT is the network modulus.

Using eqs. (6) and (7) the selected experimental true stress-true strain curves were fitted in the true strain range of $e = 0.2$–2.5. The parameters of the fit were a disposable flow stress σ_{fl}, the effective entanglement density N_{eff}, and the number of segments between entanglements n, controlling the extensibility limit of chains in the network, $\lambda_{max} = n^{1/2}$. Exemplary results of fitting are presented in Figure 6. As in the previous study,[15] the obtained fits appeared reasonably good up to the true strain of $e = 1.5$–2, well within strain-hardening stage. For higher strains, however, the predicted stress increased much faster than that observed experimentally. This discrepancy must be accounted for all simplifying assumptions done for calculations, especially that replacing the viscoplastic stress with a constant flow stress and neglecting the relaxation of the network or stress-induced crystallization, or stress-induced crystallization, which phenomena can influence significantly the stress response at the highest strains. Because of all model simplifications, the obtained results must be considered qualitatively, to be used only for a rough comparison of the behavior of samples tested at similar conditions.

Table III presents fit parameters, calculated for samples deformed at 155°C, and the strain rate of 0.001 s^{-1}. These results suggest that the effective network density which manifests in the melt compression experiment is the highest in G-M, lower in G-S, and definitively the lowest in P-S samples. At the same time the limit of chain extensibility of the initial network $\lambda_{max} = n^{1/2}$ increases from G-M to G-S and is the highest in the P-S sample. Similar relations were also found for samples deformed at 145°C and those deformed with lower strain rate of 0.001 s^{-1} at both temperatures. Such a behavior agrees well with the topological structure of the melt expected for these samples: an entangled melt near equilibrium in samples G-M, partially disentangled melt in G-S and a highly disentangled melt in P-S material.[20,23]

It must be noted that the derived values of network strain hardening modulus or entanglement density are one order of magnitude lower than those estimated from rheological measurements (plateau modulus), giving G_n and N_e around 2.5 MPa and 4×10^{26} m^{-3}, respectively, for an entangled PE melt at $T = 160$°C.[31,32] This discrepancy, as already discussed, results probably from all simplifying assumptions of the model.

Orientation of crystalline phase

Large-strain deformation of molten samples produces some, usually high, orientation of polyethylene chains along the FD. High orientation under load frequently triggers the stress-induced crystallization phenomena and consequently the formation of metastable crystals oriented along FD. On unloading, these crystals melt, while the relaxation in the melt leads to the gradual loss of the molecular orientation. That molecular orientation, however, can be at least partially preserved by fast cooling the material down, still under load. Orientation of crystallites formed on cooling reflects then quite well the molecular orientation of the melt attained on compression since partial relaxation of the melt occurring in a

TABLE III
Network Parameters Derived from Fitting of Stress–Strain Curves of Samples Deformed with the Strain Rate $\partial e/\partial t = 0.01\ s^{-1}$ at Various Temperatures

Sample	Network modulus, $N_e kT$ (MPa)	Entanglement density, $N_e \times 10^{-26}$ m^{-3}	Chain extensibility limit, $\lambda_{max} = n^{1/2}$
G-M-15	0.13	0.23	6.2
G-S-155	0.12	0.20	6.9
P-S-155	0.08	0.13	16.1

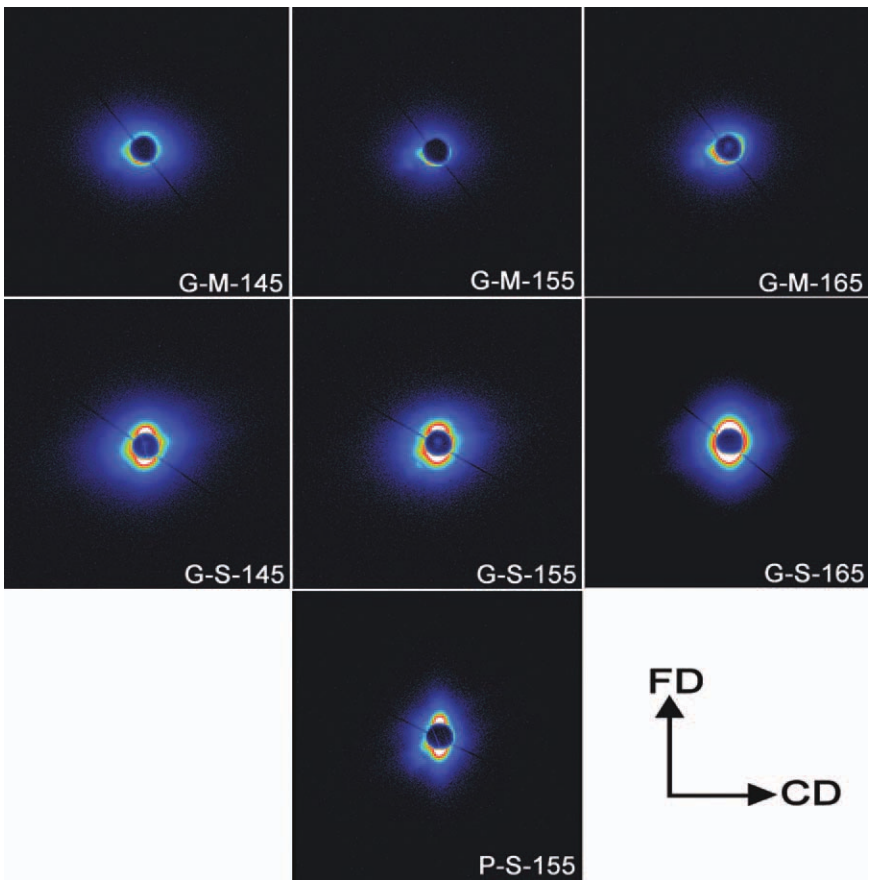

Figure 7 SAXS patterns of the samples deformed in the molten state and subsequently crystallized on cooling under load. Sample type and temperature of deformation indicated. Strain rate de/dt = 0.001 s^{-1}. Patterns recorded with illumination along the loading direction, LD. [Color figure can be viewed in the online issue, which is available at wileyonlinelibrary.com.]

short time period prior to crystallization does not reduce this orientation markedly. Additionally, at least a part of metastable crystals formed during compression and stabilizing the orientation of chains in the neighboring melt can survive the stage of cooling under load and act then as nuclei for a new oriented crystalline phase.

To study the material's orientation, the samples just deformed in the molten state were left under load and cooled down to the room temperature till completion of crystallization. The orientation of the resultant crystalline phase was probed in these samples with 2-D SAXS and WAXS (pole figures) measurements.

Figure 7 presents 2-D SAXS patterns recorded along the loading direction, LD for samples deformed at various temperatures and the stain rate of $de/dt = 0.001\ s^{-1}$. The patterns obtained for melt-processed G-M samples deformed at any temperature show an uniform diffuse scattering. Radial sections of these patterns do not exhibit any clear maximum, therefore, the long period cannot be estimated. Moreover, any feature related to the oriented lamellar structure cannot be found here, in SAXS patterns of G-M samples. A beam-specific artifact, not related to the sample structure, can be recognized only on the left-hand side of all patterns. On contrary, samples obtained by melt deformation of the sintered nascent powder, G-S, and subsequent crystallization under load produce sharp two-point SAXS patterns, which clearly indicate well developed oriented lamellar structures with lamella normals oriented preferentially along the direction of flow, FD. This means an orientation of the fold surfaces of lamellae preferentially in the LD-CD plane, perpendicular to the FD. Comparing the patterns obtained for G-S samples deformed at various temperatures one can notice some sharpening of 2-point patterns, i.e., progress of lamellae orientation with an increasing temperature of deformation. Lamellar orientation of samples deformed at 165°C looks the strongest. This seems reasonable, as the sample deformed at 165°C attained the highest true strain, $e \sim 5$ [cf. stress–strain curves of Fig. 5(a)], thus the strongest molecular orientation could be expected in this sample. The deformed sample of the significantly disentangled melt, P-S, also exhibit a 2-point SAXS pattern, with high intensity of scattering, yet not as clear and sharp as in the case of G-S samples. This pattern indicates again the

TABLE IV
Herman's Orientation Factor Calculated from X-Ray Diffraction Data and Thermal Properties of the Crystalline Phase Determined from DSC for Samples Compressed in the Melt

Sample	Preparation	Deformation temp. (°C)	f_c	T_m (°C)	X_c (wt %)
G-M	Molded at 220°C	–	0	132.8	48.9
G-M-22	Molded at 220°C	22	0.38	132.7	46.0
G-M-80	Molded at 220°C	80	0.39	132.9	44.6
G-M-145	Molded at 220°C	145	0.80	138.8	51.0
G-M-155	Molded at 220°C	155	0.45	138.2	61.0
G-M-165	Molded at 220°C	165	0.23	131.5	50.0
G-S	Sintered at 130°C	–	0	144.5	69.0
G-S-145	Sintered at 130°C	145	0.75	138.0	53.4
G-S-155	Sintered at 130°C	155	0.84	137.6	59.3
G-S-165	Sintered at 130°C	165	0.23	132.6 (m)* 136.4 (s)*	58.7
P-S	Sintered at 100°C	–	0	142.7	84.6
P-S-155	Sintered at 100°C	155	0.84	135.7 (m) 142.9 (s)	56.2

(*)–m, the main melting peak; s, secondary peak on the high temperature slope of the main peak.

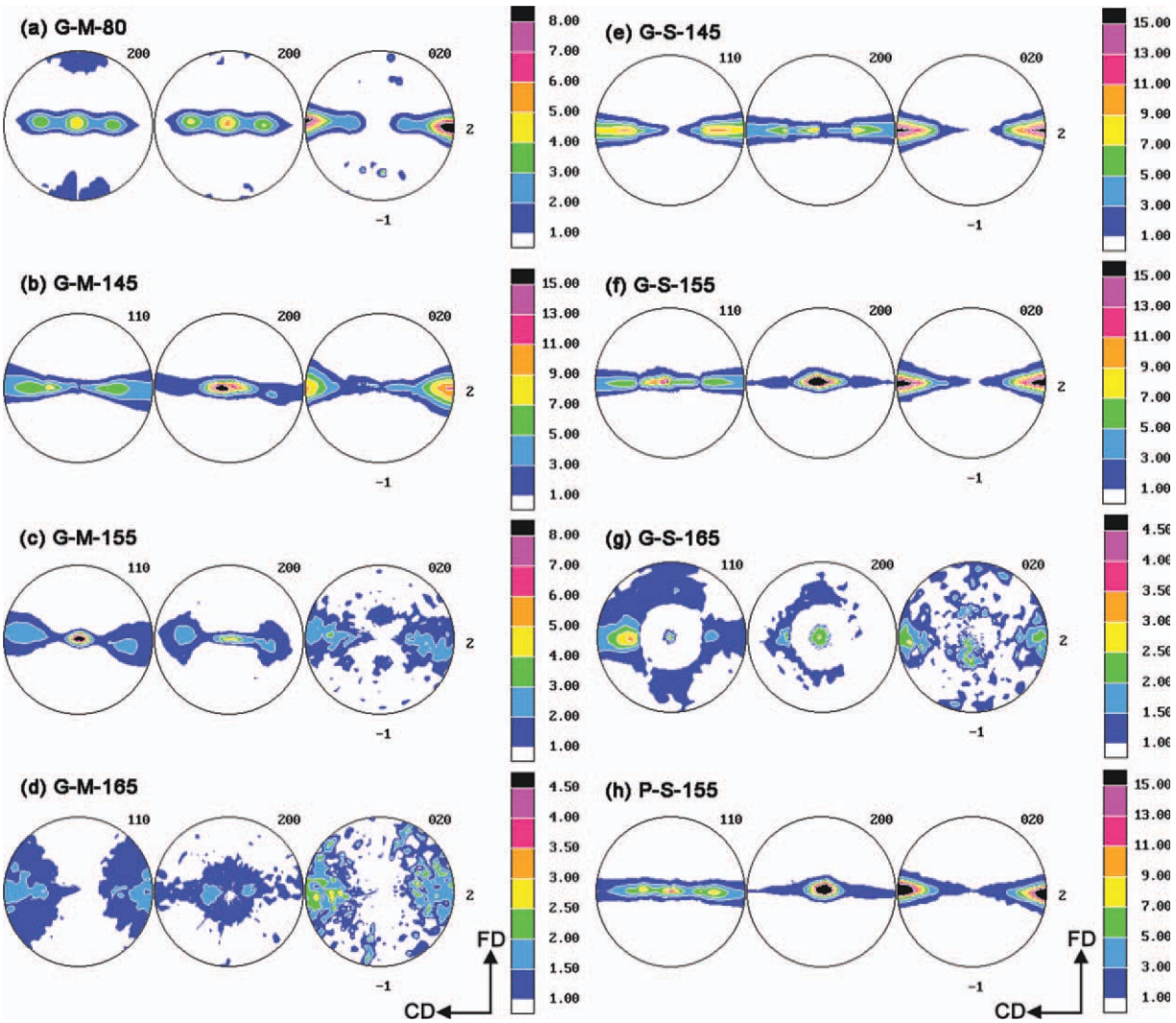

Figure 8 Representative pole figures of samples crystallized on cooling under load after deformation at the temperature indicated and the true strain rate of $de/dt = 0.001\ s^{-1}$. For every sample 3 pole figures determined for (110), (200) and (020) planes of orthorhombic PE are presented. Note different scale for each set of pole figures. [Color figure can be viewed in the online issue, which is available at wileyonlinelibrary.com.]

preferred orientation of lamellae with their normals along FD, as in G-S samples. Attempts of calculation of the long period for these lamellae failed since the maximum of the intensity was observed along FD practically just on the edge of the beam-stop. Therefore, only a lower estimate of LP above 35 nm in all G-S and P-S samples can be given. This estimate is higher than LP = 33 nm observed in the undeformed G-M sample crystallized from the melt, which indicates lamellae in samples crystallized from the deformed melt noticeably thicker than in samples crystallized from a quiescent melt. This conclusion can be supported by the melting data reported later (cf. Table IV).

Figure 8 shows representative pole figures of samples deformed in the molten state at various temperatures and the strain rate of $de/dt = 0.001\ s^{-1}$. As a reference a set of pole figures determined for G-M sample deformed in the solid state at $T = 80°C$ is also presented [Fig. 8(a)]. Each set of pole figures contains three normalized pole figures constructed for the (110), (200), and (020) crystallographic planes of orthorhombic polyethylene, respectively. All pole figures were plotted in the stereographic projection and linear scale in which numbers denote multiples of the intensity of the random distribution. The vertical direction coincides with the flow direction, FD while horizontal with the CD. The LD is perpendicular to the projection plane.

Pole figures determined for samples deformed by plane-strain compression in the solid state (deformation temperature 20–120°C) reveal usually the two-component texture consisting of the (100)[001] primary component and its {310} twin.[33] This texture is illustrated by pole figures of the G-M-80 sample deformed at 80°C, shown in Figure 8(a). Such a two-component texture is a result of activity of the (100)[001] crystallographic slip, being the main deformation mechanism, and twinning of oriented crystals, which occurs on sample unloading.[33]

On contrary, samples deformed in the melt and crystallized then on cooling under load demonstrate basically an one-component texture of the type (100)[001], i.e., a texture in which the (100) planes are oriented preferentially in the FD-CD plane (plane normals oriented preferentially along the LD) and the direction of the crystallographic **c** axis, coinciding with the direction of the chain in crystal, oriented along the flow direction, FD. Only the sample deformed at 155°C, G-M-155 reveals a weak {310} twin component in addition to the main (100)[001] texture component. In other samples this component is barely seen. Comparing pole figures obtained for melt-processed G-M samples deformed at various temperatures [cf. Fig. 8(b–d)] one can conclude that the strength and sharpness of the texture is the highest for $T_{def} = 145°C$ and decreases markedly with increasing temperature of deformation—the intensity at maxima in figures determined for G-M-145 is about 15 times greater than the intensity of the random distribution (15 m.r.d.), while for G-M-165 the maximum intensity is only about 3m.r.d. The preferred orientation of the chain axis in crystallites along the FD direction reflects the molecular orientation along FD produced by the deformation of the melt in the plane-strain compression. As the stress-induced crystallization probably occurred in the final stage of the deformation process (especially at $T_{def} = 145$ and 155°C when high stresses were generated) the metastable oriented crystals formed then could survive in the sample being still under load and act later, at lower temperature, as nuclei for the oriented crystallization. This should markedly increase the crystallization rate in samples deformed at lower temperature prior to cooling down. On the other hand, the oriented chains in the deformed melt relax and gradually loose their orientation with time when deformation is stopped. Then, the probability of nucleation and growth of the crystal oriented along initial molecular direction, i.e., FD, decreases with time. Moreover, the relaxation is faster at higher temperature while the time needed to reach crystallization temperature on cooling after the end of the deformation at that high temperature is longer than when cooling from a lower deformation temperature. All this leads the orientation of the crystals grown on cooling to decrease with an increasing temperature of the deformation process. Such features are indeed observed in the series of G-M samples.

The texture observed in the sintered powder sample deformed at 145°C, G-S-145 [see Fig. 8(e)] is again the one-component (100)[001] texture of the strength and sharpness comparable to or slightly higher than that observed in the G-M-145 sample deformed at the same temperature [Fig. 8(b)]. Similar, yet even stronger texture was determined for sample G-S-155, deformed at $T_{def} = 155°C$. Note, that texture of this sample is about twice stronger than the texture of G-M-155 deformed at the same conditions [intensity of the strongest maxima about 15 m.r.d. and 8 m.r.d., respectively; cf. Fig. 8(f and c)]. The larger strength and sharpness of the texture of G-S-145 than of G-M-145 and especially G-S-155 than of G-M-155 reflects a different topology of the melt in G-S and G-M samples, manifesting in reduced entanglement density of the molten G-S material as compared to G-M. That reduced entanglement density apparently makes chain orientation easier which enhances the final molecular orientation and consequently the orientation of grown crystallites. Similarly to the G-M series, the texture of the G-S-165 sample, deformed at 165°C, is significantly weaker than in samples deformed at lower temperatures and is quite similar to the texture of

the G-M-165 sample, indeed [cf. Figs. 8(g and d)]. The weakening of the crystallite orientation is probably again due to faster relaxation at 165°C than at lower deformation temperatures and additionally longer time needed to reach the crystallization temperature on cooling after the end of the deformation process.

Figure 8(h) presents a set of pole figures determined for the sintered sample P-S-155 deformed at 155°C and then crystallized on cooling under load. This sample of highly reduced entanglement density developed the strong and sharp one-component texture similar to that observed in G-S-155 and of comparable strength.

Comparing textures developed in samples studied one can find that all samples deformed in the melt and then crystallized on cooling under load demonstrate the same type of the texture, which is the (100)[001] one-component texture. The strength of the developed texture depends on the topological structure of the sample and the temperature of deformation. Generally, the strongest texture was observed in samples of sintered powder materials, i.e., those exhibiting reduced density of entanglements after their melting. Among those the strongest texture was developed in samples deformed at 155°C. Above qualitative conclusion can be confirmed by comparison of Herman's orientation factor of discussed samples, calculated for the crystallographic **c** axis (equivalent to chain axis in PE) with respect of the FD. That orientation factor was calculated with eqs. (2)–(4) from the same WAXS data already used for construction of pole figures. Note that $f_c = 0$ for a random orientation and $f_c = 1.0$ for a perfect orientation of **c** axis along FD. The results of calculations are presented in Table IV. They demonstrate that molded samples deformed at 145°C as well as sintered samples deformed at 145°C or 155°C exhibit very high orientation, with f_c around 0.8. The orientation factor for these samples is much higher than for samples deformed in the solid state (below the melting point). For samples with reduced entanglement density (sintered powder samples G-S and P-S) the deformation temperature of 155°C seems again to be an optimum temperature to produce the highest orientation.

Table IV reports, additionally, the temperature of the melting peak and crystallinity degree determined from DSC heating scans of deformed samples. It can be found that melting temperature of samples deformed at 145 and 155°C is very high (T_m = 137–138°C), which reflects a structure consisting of relative thick crystals, probably constrained additionally by stretched network of entangled chains of amorphous phase which leads to an apparent increase of the melting point (superheating effect). Such constraints perhaps also give rise to the formation of a secondary melting peak at very high temperature observed in few samples. Melting temperature of samples deformed at 165°C decreases to 132–133°C, a range typical for UHMWPE crystallized from the melt. This can be attributed to fewer constrains imposed on crystals by an amorphous surrounding as the chains had more time to relax on cooling, between deformation and crystallization temperatures, as compared to samples deformed at or below 155°C.

Similarly to the orientation developed in deformed materials also the crystallinity is the highest in samples crystallized after the deformation at 155°C, although for sintered powder samples it is still lower than in the nascent material before melting, deformation and recrystallization. The high crystallinity together with high orientation of formed crystals reflects high and relative stable molecular orientation in the melt produced by deformation at this temperature (due to, e.g., presence of metastable crystals formed under load and/or some topological constraints in the stretched network of entangled chains which hinder the relaxation processes), especially in samples with reduced number of entanglements G-S and P-S.

CONCLUSIONS

The results obtained in the reported study allow to draw the following conclusions:

- Molten samples of UHMWPE demonstrate in a certain temperature range (~ 145–155°C) a rubber-like behavior and can be deformed by plane-strain compression to high true strains, e = 3–4 ($\lambda > 50$) without fracture. The ultimate strain is much higher than on deformation in the solid state ($e < 1.6$, $\lambda < 5$). When the temperature of deformation is high, 165°C or above deformation of the melt becomes unstable and the molten sample exhibits microfracture phenomena already at low strain, below $e = 1$. These small fissures most frequently heal on further compression, yet the sample does not show the strain hardening behavior, very pronounced in deformation at lower temperatures.
- The ability to large deformation of the melt depends on the initial structure of the material prior to its melting—samples obtained by compaction of nascent powder, containing original nascent crystals, can deform after melting to significantly higher strains than compression molded samples, containing initially conventional folded crystals.
- The key factor controlling deformability of the UHMWPE melt is molecular network characterized by the density of chain entanglements, significantly lower in nascent samples, especially those polymerized with homogeneous catalyst at low temperature. The lower the entanglement

density the higher the ultimate strain in the plane-strain compression of a molten material.

- Due to instability of deformation at high temperatures the molecular orientation produced in samples compressed at 165°C is smaller than that in samples deformed in a stable way at or below 155°C. The final orientation observed in solidified sample is additionally reduced by intense relaxation phenomena on cooling from 165°C down to the crystallization temperature, which eventually leads to formation of crystals with more random orientation.
- Much more of the molecular orientation produced by the deformation process survives shorter cooling in samples compressed earlier at lower temperatures (145–155°C). This results in formation of highly oriented crystalline phase, especially in samples exhibiting reduced entanglement density obtained by melting of nascent powders and then deformed then at $T = 155$°C.
- The obtained results open a new route of the processing of UHMWPE for products of high orientation. The plane-strain compression of the molten slab or tape produced by compaction of a nascent powder can be thought as a first stage in the process of fabrication of ultra-strength UHMWPE fibers and/or tapes. Such a process can be highly competitive to the gel-spinning process, commonly used nowadays for production of such fibers.

References

1. Lemstra, P. J.; van Aerle, N. A. J. M.; Bastiaansen, C. W. M. Polym J 1987, 19, 85.
2. Bastiaansen, C. W. M.; Meijer, H. E. H.; Lemstra, P. J. Polymer 1990, 31, 1435.
3. Lemstra, P. J.; Bastiaansen, C. W. M.; Rastogi, S. In Structure Formation in Polymeric Fibres; Salem, D. R., Ed.; Hanser: Munich, 2000.
4. Schrauwen, B. A. G.; Janssen, R. P. M.; Govaert, L. E.; Meijer, H. E. H. Macromolecules 2004, 37, 6069.
5. Maxwell, A. S.; Unwin, A. P.; Ward, I. M. Polymer 1996, 37, 3293.
6. Smith, P.; Chanzy, H. D.; Rotzinger, B. P. Polym Commun 1985, 26, 258.
7. Scheirs, J.; Kaminsky, W. Metallocene-Based Polyolefins: Preparation, Properties and Technology; Wiley: Chichester, 2000.
8. Joo, Y. L.; Han, O. H.; Lee, H. K.; Song, J. K. Polymer 2000, 41, 1355.
9. Joo, Y. L.; Zhou, H.; Lee, S. G.; Lee, H. K.; Song, J. K. J Appl Polym Sci 2005, 98, 718.
10. Rotzinger, B. P.; Chanzy, H. D.; Smith, P. Polymer 1989, 30, 1814.
11. Kanamoto, T.; Okama, T.; Tanaka, K.; Takede, M.; Porter, R. S. Polymer 1987, 20, 1517.
12. Rastogi, S.; Kurelec, L.; Cuijpers, J.; Lippits, D.; Wimmer, M.; Lemstra, P. J. Macromol Mater Eng 2003, 288, 964.
13. Rastogi, S.; Spoelstra, A. B.; Goosens, J. G. P.; Lemstra, P. J. Macromolecules 1997, 30, 7880.
14. Lippits, D. R.; Rastogi, S.; Talebi, S.; Bailly, C. Macromolecules 2006, 39, 8882.
15. Bartczak, Z.; Kozanecki, M. Polymer 2005, 46, 8210.
16. Wunderlich, B.; Czornyj, G. Macromolecules 1977, 10, 906.
17. Alexander, L. E. X-Ray Diffraction Methods in Polymer Science; Wiley-Interscience: New York, 1969.
18. Bartczak, Z.; Argon, A. S.; Cohen, R. E. Macromolecules 1992, 25, 5036.
19. Wilchinsky, Z. W. J Appl Phys 1960, 31, 1969.
20. Lippits, D. R.; Rastogi, S.; Hohne, G. W. H.; Mezari, B.; Magusin, P. C. M. M. Macromolecules 2007, 40, 1004.
21. Cook, J. T. E.; Klein, P. G.; Ward, I. M.; Brain, A. A.; Farrar, D. F.; Rose, J. Polymer 2000, 41, 8615.
22. Ferry, J. D. Viscoelastic Properties of Polymers, 3rd edn.; Wiley: New York, 1980.
23. Rastogi, S.; Lippits, D. R.; Peters, G. W. M.; Graf, R.; Yao, Y.; Spiess, H. W. Nat Mater 2005, 4, 635.
24. Lee, B. J.; Argon, A. S.; Parks, D. M.; Ahzi, S.; Bartczak, Z. Polymer 1993, 34, 3555.
25. Bartczak, Z. Polymer 2005, 46, 10339.
26. Lemstra, P. J.; Bastiaansen, C. W. M.; Meijer, H. E. H. Angew Makromol Chem 1986, 145/146, 343.
27. van Aerle, N. A. J. M.; Lemstra, P. J. Polym J 1988, 20, 131.
28. Haward, R. N.; Thackray, G. Proc R Soc Lond A 1967, 302, 453.
29. Haward, R. N. Polymer 1999, 40, 5821.
30. Arruda, E. M.; Boyce, M. C. J Mech Phys Solids 1993, 41, 389.
31. Cassagnau, P.; Montfort, J. P.; Martin, G.; Monge, P. Rheol Acta 1993, 32, 156.
32. Pearson, D. S.; Fetters, L. J.; Graessley, W. W.; Strate, G. V.; von Meerwall, E. Macromolecules 1994, 27, 711.
33. Bartczak, Z.; Lezak, E. Polymer 2005, 46, 6050.